



# Mathematical modelling and parameter classification enable understanding of dynamic shape-change issues adversely affecting high energy-density battery metal anodes

Benedetto Bozzini<sup>a,\*</sup>, Elisa Emanuele<sup>a</sup>, Jacopo Strada<sup>a</sup>, Ivonne Sgura<sup>b</sup>

<sup>a</sup> Department of Energy, Politecnico di Milano, via Lambruschini 4, 20156, Milano, Italy

<sup>b</sup> Department of Mathematics and Physics, University of Salento, via per Arnesano, 73100, Lecce, Italy

## ARTICLE INFO

### Keywords:

Battery  
Zinc  
Anode shape change  
Battery degradation  
Battery modelling  
Coin cell

## ABSTRACT

Owing to the difficulty of studying materials in real-life battery context, research on metal anodes, suffers from a methodological gap between materials- and device-orientated studies. This gap can be bridged by quantitatively linking the electrical response of the device to the evolution of the material inside the cell. The capability of establishing this link, on the one hand, allows to frame the correct space- and time-scales that are relevant to device research and, on the other hand, helps pinpoint the global observables that can be associated with molecular-level information and imaging. This study contributes to the construction of a conceptual platform, that will enable to rationalize the electrical response of the device on the basis of materials-relevant quantities. To this aim: (i) we have developed a PDE-based mathematical model for the response of a single symmetric cell with metal electrodes; (ii) we have validated it with high-quality data from Zn/Zn symmetric coin-cell cycling in weakly acidic alkaline aqueous electrolyte, containing quaternary ammonium additives, and (iii) we have carried out a parameter-classification task for the experimental data, that notably extended the physico-chemical insight into the mechanism of action of anode-stabilizing additives.

## 1. Introduction

The ever-growing demand of electrical energy call for higher awareness for ethical, environmental, societal and political issues, raised by the usage of fossil fuels. Renewable energy sources, in practice, mainly solar and wind, can in principle replace the hydrocarbon-based protocol, but sustainability imposes their integration with safe, efficient, reliable and sustainable electrical energy storage facilities. Concretely, electrochemistry - batteries in particular -, will play the key role in building the definitive network of electrical energy storage devices in the whole power range, from mW to MW.

Batteries, even though it is tempting to regard them as straightforward commodity goods, are in fact highly complex systems, owing their operation to the synergy of several sophisticated functional components, that have to work in concertation, to ensure appropriate operation of the whole device. The constituents that actually originate energy storage are the two electrodes, the chemistry of which controls the device voltage, and the electrolyte, putting in chemical contact the two electrodes. The electrodes are connected to the external battery terminals and form a

large proportion of the device volume, the rest of which is mainly taken by the electrolyte. This electrode/electrolyte combination is essentially a device implementing an appropriate oxidation–reduction (or “redox”) reaction, implemented in a way that the reduction and oxidation half-reactions are kept separated in space and localized at the two electrode/electrolyte contacts. In order to enable the completion of the redox reaction, and consequently operation at steady-state, the reaction products generated in the individual reduction and oxidation processes, have to be brought together: the component carrying out this task is the electrolyte. Generally, the reaction products generated at the electrode are ionic in nature, and in order to allow their transport from one electrode to the other one, electrolytes must be ionic conductors. Batteries can implement redox reactions in two main modes: in an irreversible one, whereby the battery can be used only for one discharge process (primary or disposable batteries) and a reversible one, allowing discharge-charge cycles (secondary or rechargeable batteries): of course only the latter type is of interest for energy storage, and we shall concentrate on these devices.

Electrochemistry, of course, involves chemical reactions that are

\* Corresponding author.

E-mail address: [benedetto.bozzini@polimi.it](mailto:benedetto.bozzini@polimi.it) (B. Bozzini).

<https://doi.org/10.1016/j.apples.2022.100125>

Received 22 October 2022; Accepted 23 December 2022

Available online 11 January 2023

2666-4968/© 2023 Published by Elsevier Ltd. This is an open access article under the CC BY-NC-ND license (<http://creativecommons.org/licenses/by-nc-nd/4.0/>).

combined with electrical phenomena, in the previous paragraph we have concentrated on the chemical side, in the following we shall provide some information regarding the corresponding electrical phenomena.

As far as the electrodes are concerned, as stated above, they support reduction and oxidation reactions: the former correspond to flow of electrons into the battery through the negative electrode, called cathode, while the latter correlates with flow of electrons from the battery through the positive electrode, denominated anode. Electrons reaching the cathode are taken up either by the electrode material (e.g. cobalt in the most common lithium-ion batteries or manganese(IV) oxide in an alkaline ones) or by some other reagent brought in contact with it (e.g. dioxovanadium(V) ions in vanadium flow batteries or air in a button cell for hearing-aid appliances). At the anode, in turn, electrons are released from the electrode material (e.g. a lithium-carbon alloy in lithium-ion batteries or zinc in alkaline batteries) or from some other material placed in contact with it (e.g. a lead(II) salt dissolved in the electrolyte of a lead-acid battery or hydrogen in a fuel cell).

An ideal electrolyte can be any material, that does not react in brought in contact with the electrodes, able to favour the flow of ions and electronically insulating, in order to prevent internal short-circuit of the electrodes. Electrolytes can be liquids (both aqueous and non-aqueous), ceramics, glasses, polymers or multi-phase combinations of them.

Regarding the chemistries that can be implemented in battery chemistries, it is hardly possible to even list those that have been proposed in over two centuries of literature, nevertheless, they can be classified into three main types, according to the physical nature of the redox-active materials. We can thus distinguish amongst batteries with: (i) insertion electrodes; (ii) conversion electrodes and (iii) reactive species dissolved in the electrolyte. Insertion means that the electrochemical reaction leads to the incorporation of ions into a host material: this is the type of mechanism involved in state-of-the-art rechargeable lithium-ion and lithium-polymer batteries. At conversion electrodes the electrochemical reaction leads to the formation of a new phase: this approach is employed in lead-acid, nickel-cadmium and nickel metal-hydride batteries. The better-known technology implementing redox reactive species dissolved in the electrolyte are the redox-flow batteries, in particular those using different forms of vanadium. Regarding batteries with conversion electrodes, it is worth noting that they are the most promising systems in view of developing of high energy- and power-density devices that are required especially for mobility, in particular if metallic anodes are used (Han et al., 2021; Yang et al., 2020; Zhu et al., 2020). Unfortunately, the only currently commercially available technology of this type are lead-acid batteries, using extremely heavy lead. One of the key development areas in battery research is thus finding ways to use metallic anodes, ideally of light elements, avoiding lithium, that is pyrophoric and sourced only in potentially critical geopolitical areas. Post-Li metal candidates that are closer to applications are Zn and Mg, while Ca and Na are important, but more complex alternatives (Li et al., 2020; Palacín and Ponrouch, 2019; Ponrouch et al., 2019). Unfortunately, use of metal anodes is impaired by poorly understood shape changes, leading to various, potentially dangerous, failure modes: mainly capacity fade and electrode shorting (Zhao et al., 2018; Dasgupta et al., 2017; Higashi et al., 2016).

In spite of a time-honoured tradition of fundamental and applied studies on Zn electrodeposition (Chen et al., 2021) and corrosion (Sun et al., 2022; Sun et al., 2020), addressed separately in different fields of technology, and the recent publication deluge, mainly on Li (Gallant et al., 2022; Minguzzi et al., 2022; Yang et al., 2021; Zhu et al., 2020), Zn (Wang et al., 2023; Kheawhom et al., 2022; Liang et al., 2021; Ling et al., 2020) and Mg (An et al., 2022; Yu et al., 2022; Zeng et al., 2021), but also on Na (You et al., 2021; Ma et al., 2020; Stucky et al., 2020) and Ca (Liu et al., 2022; Mai et al., 2022), practical ways to control morphology changes accompanying cycling in real battery ambient have not been discovered, as evidenced by the fact that no devices based on these

materials have reached the market, yet. Certainly, one of the reasons of this situation is that the largest proportion of published work is empirical, is accompanied by common-sense physico-chemical justification, rather than by predictive formalized modelling, and quite often modifications of materials and operating conditions, that are sought with a trial-and-error approach, lack fully verifiable and statistically robust experimental validation. For this reasons, deepening fundamental aspects and, in particular, providing a firm physico-mathematical background is particularly crucial for rational advancements in the field. From the battery materials science and engineering viewpoint, this paper is focussed on morphochemical changes occurring at metal electrodes as a result of applied electrochemical polarization.

The understanding of the mentioned shape-change issues can be fostered only through the establishment of a cogent link between experimental electrochemical materials issues and their rationalization based mathematical modelling of electrochemical phase growth. Several attempts in this direction have been described in the literature, the success of which has been only partial because, on the one hand, most models proposed lack predictive power and, on the other hand, the description of the impact of anode shape changes at the device-response level has been neglected. It is worth, first briefly recalling here – without claim of completeness – the most representative literature approaches and then sketching on this literature background. Early work in the field relied on phenomenological kinetics and described unstable growth as entirely controlled by electrochemical reaction kinetics (Diggle et al., 1969). This effective, but crude approach was soon improved by accounting for mass-transport effects (Popov et al., 2002). Moreover, metal growth shapes controlled by the aggregation of nanoclusters aggregation was described combining diffusive mass transport with simple geometrical assumptions (Desai et al., 2014). Incorporation of mass-transport and nucleation phenomena inspired modelling approaches beyond algebraic ones. Statistical approaches have been adopted to model phase formation through diffusion-limited aggregation (Chen and Jorne, 1990) and Montecarlo (Lucas and Moskovkin, 2010) approaches. Moreover, mass-transport impact on unstable metal electrodeposition has been modelled with the joint density functional method (Lu et al., 2014). Differential modelling has indeed played a key methodological role, even though it has so far attained limited success in terms of capability of describing real morphologies and predictive power. Early studies proposed an electrochemical extension of the Mullins-Sekerka theory, adding an electrochemical potential gradient (Hamilton, 1963). This approach has been refined with reaction-diffusion modelling, solving for the case of concentration distribution of two chemicals and describing shape change through the boundary conditions (Chazalviel, 1990). This multiphysics approach has been further extended by incorporating ionic transport by diffusion, migration and convection, solving simultaneously equations for reaction-diffusion, electric field and fluid-dynamics (Wang et al., 2014). Over the past decade some of the Authors have developed a reaction-diffusion PDE-based approach, able to capture the essential features of unstable material growth in electrochemical systems (Lacitignola et al., 2015; Bozzini et al., 2015; Lacitignola et al., 2014; Bozzini et al., 2013): recharge instability problems in batteries with metal anodes are a special case of this phenomenon. According to this approach, the source term for morphology accounts for charge-transfer rate at sites free from adsorbates, mass-transport hindrance to metal growth and the impact of adsorption on electrodeposition rate. The source term for chemistry considers adsorption and desorption, controlled by both chemical and electrochemical contributions. Theoretical and numerical studies have shown the notable flexibility of the RD-PDE in following the rich of spatio-temporal electrochemical experimental patterns reported in the literature, in particular through: (i) spatial pattern formation resulting from diffusion-driven or Turing instability (Lacitignola et al., 2015); (ii) occurrence of a supercritical Hopf bifurcations and the interplay between Hopf and Turing instabilities, yielding complex spatio-temporal behaviour as well the capability of supporting

time-periodic oscillations and spiral-wave / break-up phenomena (Bozzini et al., 2015; Lacitignola et al., 2014). This model has been successfully applied for the rationalization of *post mortem* and *in operando* hyperspectral images of Zn anode morphochemical changes (B. Bozzini et al., 2022a).

As mentioned above, one of the weaknesses of state-of-the-art mathematical modelling of metal anode shape-changes is the fact that they cannot describe the impact of this process on the cell response: this work is aimed at developing an approach to tackle this issue. A related idea was put forward in Wood et al. (2016), but this solution exhibits two main drawbacks: it assumes that at each discharge-charge cycle the initial planar electrode configuration is regained, thus excluding *a priori* any kind of irreversible changes, which are the conceptual cause of the shape changes that affect the battery behaviour, the mathematical description available in the paper is not only incomplete, but also inconsistent. In B. Bozzini et al. (2022b) we proposed for the first time a model that includes both cathodic and anodic irreversibilities and demonstrated qualitatively the way this model can be used to follow experimental cell cycling experiments, postponing the mathematical details to the present publication, that not only provides the full formal and numerical framework, but also employs it to achieve a mechanistic grasp of an experimental dataset of interest in its own right for the science and technology of battery materials.

## 2. The mathematical model

### 2.1. Description of morphology evolution and passivation (included in BCs)

#### 2.1.1. Electrodeposition and corrosion geometry

The model accounts for irreversibilities (aspect neglected in Wood et al. (2016)) in two ways: (1) metal outgrowth and (2) passivation. A summary and a more detailed description of the physical meaning of the model parameters can be found in Appendix 1.

**2.1.1.1. Hemispherical growth features.** The starting point of our model is the electrodeposition/corrosion model of Wood et al. (2016). This model is rather loosely and cryptically described in the supporting information, we have independently rationalized it and made it explicit. In Wood et al. (2016) only metal outgrowth was considered, but it was handled in a way in which irreversibilities were simple neglected and build-up and removal of metal in cathodic and anodic cycles were described in terms of a population of half-spheres forming on a flat surface during the cathodic period and shrinking back to the flat initial condition during the anodic interval.

The metal mass  $M(t)$  [mol] deposited at time  $t$  is:

$$M(t) = \frac{1}{zF} \int_0^t I(\tau) d\tau \quad (1)$$

where,  $z$  [eq/mol] is the valence,  $F$  [C/eq] is Faraday's constant and  $I$  [A/s] is the applied current intensity.

Since in this work, coherently with most of the experimental accounts of symmetric cell testing in the context of battery studies,  $I(t)$  is a galvanostatic square wave of period  $T$ ,

$$M(t) = \frac{IT}{2zF} \Lambda(t; T) \quad (2)$$

where  $\Lambda(t; T)$  is the unit triangular function of period  $T$  (i.e. with vertex value of 1 at  $T \cdot ((N-1) + 1/2)$ , with  $N$  the cycle number, see Fig. 1).

Of course the volume of deposited metal  $V(t)$  [m<sup>3</sup>] is:

$$V(t) = \frac{M(t)}{\rho} = \frac{IT}{2zF\rho} \Lambda(t; T) \quad (3)$$

with  $\rho$  [mol/m<sup>3</sup>] the molar density.

Assuming, as in Wood et al. (2016) and as customary in the literature on the modelling of electrochemical nucleation (Fletcher, 1983; Sluyt-ers et al., 1987), that the deposited metal takes on the form of a hemisphere, the radius  $r(t)$  of this hemisphere is:

$$r(t) = \sqrt[3]{\frac{3IT}{4\pi zF\rho} \Lambda(t; T)} \quad (4)$$

Moreover, we assume – as implicitly done in Wood et al. (2016) – that the hemispheres are arranged on the electrode surface in a simple square array of lattice  $2r_{\max}$  (see Fig. 2). In this scheme, the growth morphology is a time- dependent one if  $0 \leq r < r_{\max}$ , while it remains constant, and the structured electrode simply translates normally the original flat surface into the electrolyte when the hemisphere radius  $r = r_{\max}$  is attained as a result of growth. The two characteristic growth regimes described by this model are sketched in Fig. 3.

For electrokinetic reasons that will be specified in Section 2.1.2, it is useful to define the fraction  $\vartheta_{\text{hs}}$  of the electrode area consisting of freshly electrodeposited hemispheres. Variations in electrode will be referred to a square area  $A_0 = 4r_{\max}^2$  of the initially flat surface. Being  $t_{\max}$  the time required to grow the hemispheres to the maximum radius  $r_{\max}$ , the area  $A_{\text{hs}}$  of the hemispherical features (of radius  $r \leq r_{\max}$ ) sitting on  $A_0$  is:

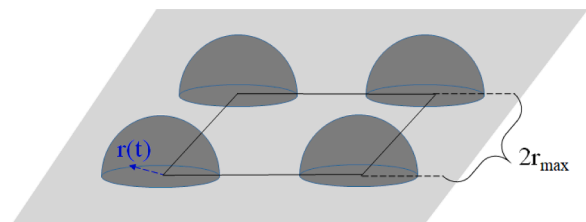


Fig. 2. Assumed geometry and arrangement of outgrowth features.

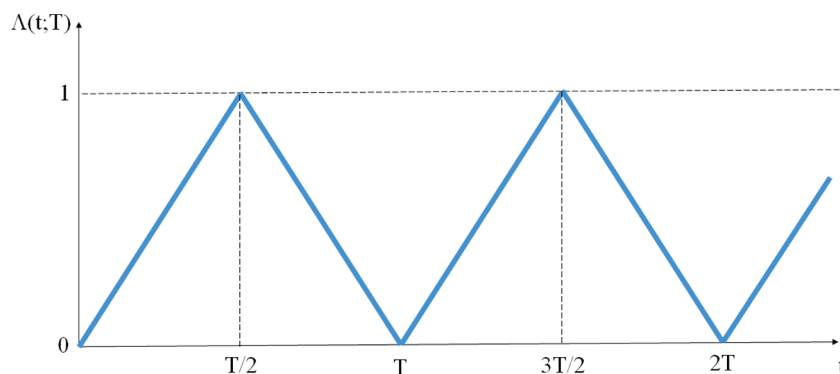
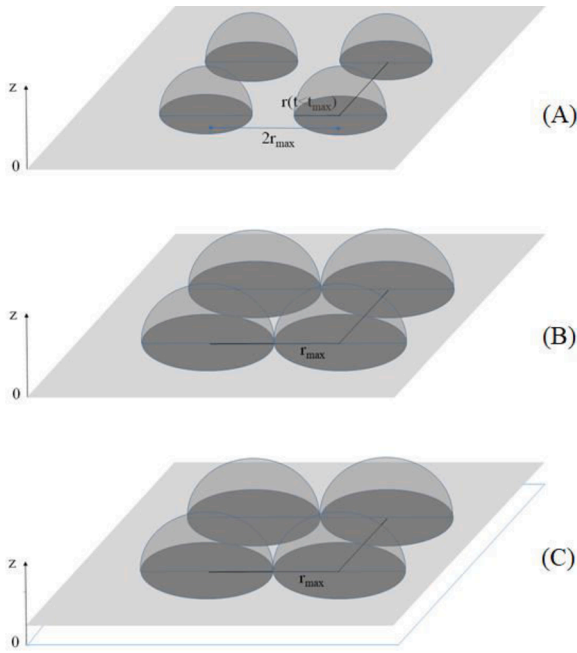


Fig. 1. Definition of the unit triangular function  $\Lambda(t; T)$ , see Eq. (3).



**Fig. 3.** Sketch of the morphology evolution and cathode growth geometry considered in the model.  $z$  is a coordinate normal to the initially flat electrode shape, the origin of which is located at the electrode/electrolyte interface at time  $t = 0$ . (A) Cathode geometry for  $t \leq t_{\max}$  and  $r_{\max} = r(t_{\max})$  (see Eq. (4)). (B) Cathode geometry at  $t = t_{\max}$ . (C) Cathode geometry at  $t > t_{\max}$ .

$$A_{hs}(t) = 2\pi r^2(t) \quad (5)$$

Thus, the residual flat area  $A_{rf}$  of the electrode surface onto which hemispheres have not formed is:

$$A_{rf}(t) = 4r_{\max}^2 - \pi r^2(t) \quad (6)$$

where, of course,  $\pi r^2$  is the area at the basis of the hemispheres on the flat support. whence  $\vartheta_{hs}$  can be defined as:

$$\vartheta_{hs}(t) = \frac{A_{hs}(t)}{A_{hs}(t) + A_{rf}(t)} = \frac{2\pi r^2(t)}{\pi r^2(t) + 4r_{\max}^2} \quad \text{for } t \leq t_{\max} \quad (7a)$$

$$\vartheta_{hs} = \frac{2\pi}{\pi + 4} \quad \text{for } t \geq t_{\max} \quad (7b)$$

It is worth recalling here that the growth interval is limited to the cathodic half period of the cathodic-anodic galvanostatic cycle:  $0 \leq t \leq T/2$ , hence if  $t_{\max} < T/2$  the growth condition represented in Fig. 3C simply cannot be attained.

**2.1.1.2. Irreversibility due to metal outgrowth.** As hinted-at at the beginning of Section 2.1, Wood et al. (2016) seems to tacitly assume that the charge consumed in both cathodic (electrodeposition) and anodic (corrosion) half-cycles only goes into mass added to/removed from the hemispheres forming during the cathodic half-cycle. This results in the fact that morphology development is reversible (i.e. hemispheres form on an initially flat surface in the cathodic half-cycle and are totally consumed in the anodic one).

Of course, this is not a realistic situation, when trying to follow the cycling of metal anodes in practically relevant condition: a model of irreversibility is thus needed. A simple way to account for irreversibilities of the “shape change” or “dendrite” type is to consider the following processes. (i) During electrodeposition new metal forms only on “outgrowth features”, modelled as hemispheres in Section 1.1, while no fresh metal deposits on the “flat” onto which the hemispheres rest. This is a rudimentary way to account for screening of current density (c.d.) lines by a growing metal feature, prototypically a dendrite (Bozzini

et al., 2012). (ii) During corrosion, instead, metal dissolves both from the outgrowth features and from the flat: this situation corresponds to the fact that active dissolution of metals tends to occur even under low anodic polarization.

Combination of the cathodic and anodic processes described in points (i) and (ii) above, leads to the fact that outgrowth features tend to build up over time, accounting for unstable shape formation.

A formal way to introduce this effect is by assigning  $F_C$ , the fraction of mass that is not corroded from hemispheres during the anodic half-cycle, but from the flat portion of the electrode. In this work  $F_C$  is assumed to be constant, for simplicity. During the cathodic half-cycle, the same amount of material is added to the hemispheres, as described in Section 1.1, i.e.:

$$M(t) = \frac{IT}{2zF} \Lambda(t; T) \quad \text{for } 0 \leq t \leq \frac{T}{2} \quad (8a)$$

Instead, during the anodic half-cycle the amount of material removed from the hemisphere  $M_{hs}$  is:

$$M_{hs}(t) = \frac{IT}{2zF} \Lambda(t; T) \cdot (1 - F_C), \quad \text{for } \frac{T}{2} \leq t \leq T \quad (8b)$$

Concretely, this means that the net corrosion current acting on hemispheres is  $I \cdot (1 - F_C)$ .

While, that corroded away from the flat background  $M_{fb}$  is:

$$M_{fb}(t) = \frac{IT}{2zF} \Lambda(t; T) \cdot F_C, \quad \text{for } \frac{T}{2} \leq t \leq T \quad (8c)$$

In other words, this means that the net corrosion current acting on the flats (i.e. not on hemispheres) is  $I \cdot F_C$ .

Assuming, for simplicity, that during removal of  $M_{hs}$  and  $M_{fb}$ , the hemispherical shape is preserved, as sketched in Fig. 4, only  $M_{hs}$  contributes to shape change.

Since  $M(T/2) > M_{hs}(T; F_C > 0)$ , the amount of material contributing to the buildup of hemispheres during the cathodic half-cycle is larger than that dissolved from the same hemispheres during the anodic one, electrodeposited hemisphere will not disappear at the end of each cycle, as in (Wood et al. (2016), were morphology is reset to the initial condition at every cycle. With our modified model, accumulation of metal in the form of hemispheres continues over cycling.

Thus, to describe the mass build-up and the radius evolution over the whole cycling time, we replace the function  $\Lambda(t; T)$  in Eq.s (2) and (4) with its corrected expressions given by Eq.s (8a) and (8b). The corresponding explicit algorithmic expression is given in Appendix 2.

### 2.1.2. Electrodeposition and corrosion kinetics

Following the approach of Wood et al. (2016), kinetics of electrodeposition and stripping is described in terms of space-independent, but time-dependent apparent exchange current densities, depending on the types of processes going on at characteristic positions on the electrode surface. In the present work, in addition to metal plating and stripping – corrected for morphology evolution over cycles (Section 1.2) –, that will be discussed in Section 2.1, we shall also include irreversibilities due to passivation, commented in Section 2.2.

**2.1.2.1. Electrodeposition and active corrosion (neither affected by passivation).** Apparent plating and stripping rates at the whole electrode, of course depend on the c.d. distribution, that in turn depends on geometrical factors giving rise to localization. A simplified approach to describing localization issues in the cathodic case is to split the active (i.e. non-passivated, for details see Section 2.2) part of the electrode in two regions: a “flat” one (quantified by  $\vartheta_{flat}$ ) and one with “hemispherical bulges” (quantified by  $\vartheta_{hs}$ , see Eq. (7a,b)). Of course, under the adopted hypotheses, in the case without outgrowth  $0 \leq \vartheta_{hs} \leq 1$  and with outgrowth  $0 \leq \vartheta_{hs} \leq 2$ . We simply model  $\vartheta_{flat}$  as  $\vartheta_{flat} = 1 - \vartheta_{hs}$ , if  $\vartheta_{hs} \leq 1$  and we set  $\vartheta_{flat} = 0$ , if  $\vartheta_{hs} > 1$ .



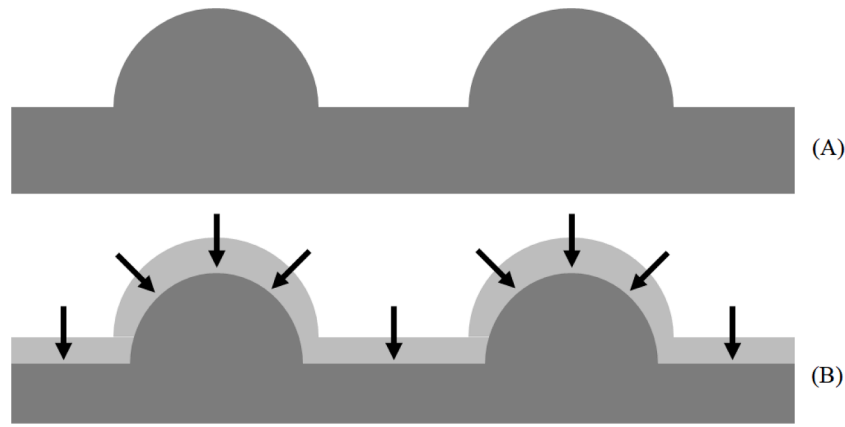


**Fig. 4.** Sketch of the morphology change resulting from the anodic half-cycle, under the hypothesis of preserved spherical shape of outgrowth features even during corrosion of the flat background (see Eq. (8)).

**2.1.2.2. Passivation.** Passivation rate depends on local c.d. distribution and, in this model, we accounted for this aspect by defining time-dependent passivation degrees for hemispherical bulges ( $\vartheta_{hs,pass}$ ) and flat regions ( $\vartheta_{flat,pass}$ ) of the electrode. Being  $t_{anod}(t)$  the total time spent in anodic conditions at time  $t$  during a given cycling experiment, we define:

$$\vartheta_{hs,pass}(t) = \int_0^{t_{anod}(t)} k_{hs,pass} \cdot \vartheta_{hs}(\tau) \cdot d\tau \quad (9a)$$

$$\vartheta_{flat,pass}(t) = \int_0^{t_{anod}(t)} k_{flat,pass} \cdot \vartheta_{flat}(\tau) \cdot d\tau \quad (9b)$$

where  $k_{hs,pass}$  and  $k_{flat,pass}$  are the passivation rates that, for simplicity, we considered constant for the hemispherical and flat regions of the electrode, respectively. The algorithm is devised in a way that  $\vartheta_{hs,pass}$  and  $\vartheta_{flat,pass}$  are set equal to 1 if the evolution of passivation were to lead to a value in excess of this physical limit.

**2.1.2.2.1. Accounting for gravitational effects.** Since passivation is related to precipitation processes, gravity can have an impact that renders the behaviour of the chemically symmetric cell in fact asymmetric owing to the fact that the electrode facing upwards is more liable to passivate owing to a gravitational contribution. This effect can be straightforwardly incorporated into the above-described passivation model by setting different values of passivation rates  $k_{hs,pass}$  and  $k_{flat,pass}$  for the upper and lower electrodes, respectively:  $k_{hs,pass}^{upper}$ ,  $k_{hs,pass}^{lower}$ ,  $k_{flat,pass}^{upper}$  and  $k_{flat,pass}^{lower}$ .

**2.1.2.3. Global kinetics from electrode geometry and passivation descriptors.** The global kinetics is thus described by a time-dependent effective kinetic constant  $k_o(t)$  that is the weighted sum of the kinetic constants  $k_{o,hs}$  and  $k_{o,flat}$ , for the active (non-passivated) portions of the electrode that are covered with hemispheres or flat, respectively:

$$k_o(t) = k_{o,hs} \cdot \vartheta_{hs}(t) \cdot (1 - \vartheta_{hs,pass}(t)) + k_{o,flat} \cdot \vartheta_{flat}(t) \cdot (1 - \vartheta_{flat,pass}(t)). \quad (10)$$

## 2.2. Description of PDE model of symmetric cell voltage response resulting from morphology evolution and passivation

### 2.2.1. The PDE system

The PDE model is inspired by Wood et al. (2016), which provides a simple and sound description of the essential physical-chemistry underlying the process, and fixes some conceptual flaws and inaccuracies contained in the original publication.

We consider a 1D, time-dependent model for the balance of metal

ions  $u$  (dimensions of  $u$ : typically  $\text{mol cm}^{-3}$ ) and for the voltage  $\phi$  (dimensions of  $\phi$ : V) of the electrolyte phase. Specifically,  $u$  is the concentration of the ions corresponding to the metal anode,  $u = [\text{Li}^+]$  in the particular case of Wood et al. (2016), but this can be generalized to any electroactive ions, such as, e.g.,  $\text{Zn}^{2+}$ .

In the driving forces of metal ion movement are diffusion and migration, their 1D flux  $J$  [ $\text{mol cm}^{-2} \text{s}^{-1}$ ] can be written:

$$J = -D \frac{\partial u}{\partial x} - \frac{zDF}{RT} u \frac{\partial \phi}{\partial x} \quad (11)$$

where:  $D$  [ $\text{cm}^2 \text{s}^{-1}$ ] is the diffusion coefficient,  $z$  [ $\text{eq mol}^{-1}$ ] is the valence,  $F$  [ $\text{C eq}^{-1}$ ] is Faraday's constant and  $R$  [ $\text{C V T}^{-1} \text{mol}^{-1}$ ] is the gas constant.

If we identify the integration domain with the electrolyte, no source term for  $u$  is present in the domain and the 1D mass balance for  $u$  can be written as:

$$\frac{\partial u}{\partial t} = -\frac{\partial J}{\partial x}. \quad (12)$$

In the absence of uncompensated charges in the integration domain, the electrical potential (voltage) distribution in the domain is given by the 1D Laplace's equation:

$$\frac{\partial^2 \phi}{\partial x^2} = 0. \quad (13)$$

The electrochemical PDE model is thus the system of Eq.s (12) and (13). This system with the BCs and ICs detailed in next Sections 2.2.3 and 2.2.4 can be solved conveniently, though not optimally in terms of computational load, with the PDEPE solver of the well known scientific program MATLAB. Details for the concrete implementation are provided in the Appendix 2.

### 2.2.2. Integration domain

As hinted at in Section 1, the 1D integration domain over space, corresponding to the electrolyte, is defined along the  $x$  [cm] axis as  $0 \leq x \leq L$ . The integration domain over time corresponds to the whole cycling time  $t$  [s] such that:  $0 \leq t \leq t_{exp}$  with  $t_{exp}$  the duration of the experiment.

### 2.2.3. Boundary conditions

At the boundaries, natural coupling conditions between the variables and on the fluxes can be given as follows.

**2.2.3.1. BCs for the coupling of the unknowns.** In order to discuss the coupling between  $u$  and  $\phi$  at the boundaries, it is useful to recall the Nernst equation, an equilibrium statement, that can be written in the present case as:

$$(\phi - \phi_M) - (\phi - \phi_M)_{st} = \frac{RT}{zF} \ln \left( \frac{a_{ion}}{a_M} \right) \cong \frac{RT}{zF} \ln \left( \frac{u}{a_M} \right) \quad (14)$$

where:  $\phi_M$  is the electrical potential of the metal phase in contact with the electrolyte, the pedex "st" refers to the standard state,  $a_{ion}$  denotes the activity of the ions, that can be approximated with the ion concentration  $u$  and  $a_M$  is the activity of the metal. Of course, at equilibrium  $u$  is independent on  $x$  and can be indicated with  $u_o$ . We shall see later (Section 2.2.4), that, in our problem, this value is, in fact, the initial condition on  $u$ . It can be straightforwardly proved that Eq. (14) holds even out of equilibrium, provided the concentration is meant as that at the electrode-electrolyte interface: we express this with  $u_{surf}$ . In correspondence, the equilibrium value of  $f$ , let us call it  $(\phi - \phi_M)_{eq}$ , is replaced by its out of equilibrium value  $(\phi - \phi_M)_{non-eq} = (\phi - \phi_M)_{eq} + \eta$ , where  $\eta$  is the overvoltage. For notational convenience we shall drop the pedex "non-eq" in the following. Since  $\phi_M$  can be regarded as constant in the system of interest, and accepting the approximation  $a_{ion} = u$ , we can rewrite Eq. (14) in the equilibrium and out of equilibrium cases as:

$$\phi_{eq} - \phi_{st} = \frac{RT}{zF} \ln \left( \frac{u_o}{a_M} \right) \quad (15a)$$

$$\phi - \phi_{st} = \frac{RT}{zF} \ln \left( \frac{u_{surf}}{a_M} \right) \quad (15b)$$

Subtracting Eq. (15a) from Eq. (15b):

$$\phi - \phi_{eq} = \frac{RT}{zF} \ln \left( \frac{u_{surf}}{u_o} \right) \quad (16)$$

Since the cell voltage is equal to the difference between the potentials in the electrolyte measured at  $x = 0$  and  $x = L$ , in the present case and, at equilibrium the cell voltage is of course zero, in this case, for simplicity, we can take  $\phi_{eq} = 0$ .

Eq. (16) can thus be recast into the expression of the BCs for the coupling of unknowns:

$$\phi(x=0, t) = \frac{RT}{zF} \ln \left[ \frac{u(x=0, t)}{u_o} \right] \quad (17a)$$

$$\phi(x=L, t) = \frac{RT}{zF} \ln \left[ \frac{u(x=L, t)}{u_o} \right] \quad (17b)$$

**2.2.3.2. BCs for the flux.** The ionic flux at the boundaries must equate, with the appropriate dimensional adjustments, the c.d.  $i(t)$ , applied in the galvanostatic experiment. Recalling Eq. (11), this writes as:

$$-D \cdot \frac{\partial u}{\partial x} \Big|_{x=0,t} - \frac{zDF}{RT} \cdot u(x=0, t) \cdot \frac{\partial \phi}{\partial x} \Big|_{x=0,t} = \frac{i(t)}{zF} \quad (18a)$$

$$-D \cdot \frac{\partial u}{\partial x} \Big|_{x=L,t} - \frac{zDF}{RT} \cdot u(x=L, t) \cdot \frac{\partial \phi}{\partial x} \Big|_{x=L,t} = \frac{i(t)}{zF} \quad (18b)$$

where, of course,  $[i/(zF)] = \text{mol cm}^{-2} \text{ s}^{-1}$ .

In order to convert the current intensity  $I$  [Amp] into the c.d.  $i$  [Amp  $\text{cm}^{-2}$ ] that is involved in the BCs on the flux, one must account for the effective electrode area. This is the nominal electrode area  $A$  [ $\text{cm}^2$ ], corresponding to the initial flat geometry, corrected for shape variations due to electrodeposition (that tend to increase the effective electrode area) and passivation (that restricts the fraction of the area over which electrodeposition, in the cathodic half-cycle, and corrosion, in the anodic half-cycle, can take place). These variations in the effective electrode area can be accounted through the effective kinetic function  $k_o(t)$ , defined in Section 2.1.2.3 (Eq. (10)). Thus:

$$i(t) = \frac{I(t)}{A \cdot k_o(t) / k_{o,hs}} \quad (19)$$

### 2.2.4. Initial conditions

Of course, ICs on the unknowns are required for the solution of the PDE model. Quite naturally, the IC for the metal ion concentration is its initial, homogeneous value  $u_o$ :

$$u(x, t=0) = u_o \quad (20)$$

The IC for the electrical potential distribution in the electrolyte is less straightforward, but a reasonable form can be assigned on the basis of the following simple physical reasoning.

Let us take  $\phi(x=0, t=0) = 0$ , meaning that the cell terminal at  $x = 0$  will be the electrical potential reference in cell voltage measurements, and  $\phi(x=L, t=0) = I \cdot L / \kappa$ , meaning that we assume the cell to behave a resistor of specific conductivity  $\kappa$  [ $\Omega^{-1} \text{ cm}$ ]. Under the same resistor assumption, we can linearly interpolate in the interval  $0 < x < L$ , resulting in the IC:

$$\phi(x, t=0) = I(t=0) \cdot \frac{x}{L} \quad (21)$$

### 2.2.5. Accounting for cell voltage

The flux BCs provide comprehensive information regarding the unknowns of the PDE system of Eq.s (11)-(13) (concentration of the electroactive species  $u$  and the potential within the electrolyte phase  $\phi$ ) in the galvanostatic case of practical interest, but are not enough to model the actual potential drop across the cell  $\Delta\Phi$ . In fact:  $\Delta\Phi = \Delta\phi + \eta_{cath} + \eta_{an}$ , where:  $\Delta\phi = |\phi(L) - \phi(0)|$ , i.e. the potential difference, within the electrolyte, between the anodic and cathodic boundaries (i.e. where the cation fluxes are directed inwards and outwards wrt the integration domain) and  $\eta_{cath}$  and  $\eta_{an}$  are the cathodic and anodic overvoltages, respectively: conventionally the absolute values of these overvoltages will be considered in the sum for  $\Delta\Phi$ . In general,  $\eta_{cath}$  and  $\eta_{an}$  can be modelled according to primary (purely ohmic control:  $\eta^{\Omega}$ ), secondary (pure charge-transfer control, typically expressed with a Butler-Volmer type equation:  $\eta^{CT}$ ) and tertiary (with combined charge-transfer and mass-transport contributions) c.d. distribution models (e.g. (Newman, 1991)).

In the system of interest (typically, a coin cell with a separator in which a liquid electrolyte is immobilized), mass-transport effects are sufficiently accounted for by the material balance equation for the electroactive species (Eq.s (11) and (12)).

Ohmic effects can be incorporated with the relation:  $\eta^{\Omega} = \frac{A}{\kappa} Li$ , where  $\kappa$  [ $\Omega^{-1} \text{ cm}$ ] is the electrolyte conductivity (Eq. (21)),  $A$  [ $\text{cm}^2$ ] is the electrode area (Eq.s (19)) and  $L$  [ $\text{cm}$ ] is the length of the 1D electrolyte domain.

Under the approximation that the anodic and cathodic Tafel slopes are equal to  $B$  - that is quite appropriate for the metals of interest for battery anodes, moreover, in a model in which possible passivation is accounted for in the BCs - one can adopt the following expression (B. Bozzini et al., 2022c):

$$\eta_{an}^{CT} + \eta_{cath}^{CT} = 2B \cdot \ln \left[ \frac{1}{2} \cdot \left( \frac{i}{i_o} + \sqrt{\left( \frac{i}{i_o} \right)^2 + 4} \right) \right] \quad (22)$$

Overall, the cell voltage can thus be written as:

$$\Delta\Phi = \Delta\phi + \frac{A}{\kappa} Li + 2B \cdot \ln \left[ \frac{1}{2} \cdot \left( \frac{i}{i_o} + \sqrt{\left( \frac{i}{i_o} \right)^2 + 4} \right) \right] \quad (23)$$

## 3. Coin-cell cycling experiments

An enabling step for the systematic quantitative investigation of cell cycling is, on the one hand, making quantitative use tendentially of all the information contained in the time-series, and, on the other hand, getting the cell mounting and cycling activities as much as possible under explicit control. In fact, explicitly addressing and removing both random and operator-dependent sources of variance in the testing of

laboratory cells, strongly increases the significance of the experiments, especially when the aim of the research is systematically assessing the impact of a given change in cell chemistry or testing conditions. To this aim, 100% control of the fabricated cells has been performed by electrochemical impedance spectroscopy, that enabled the rejection of items displaying anomalies in their electrochemical behaviour and two cells yielding sound and identical impedance behaviour have been selected for cycling tests.

The experimental case addressed in this work is establishing a link between electrochemical behaviour upon cathodic/anodic cycling and a morphology evolution of Zn foils, in weakly acidic aqueous electrolytes. This electrolyte is the system of choice in ZIB research, that is also starting to be considered for Zn-air batteries. To this aqueous electrolyte, organic species were added, with the aim of suppressing the formation of unstable growth, mainly mossy Zn: the most relevant form in the c.d. range of interest for battery operation. An ideal additive should prevent the formation of non-compact structures, suppress corrosion, and avoid passivation – thus increasing cell lifetime –, without appreciably impacting discharge and charge rates. The electrochemical behaviour of additives under combined charge and discharge conditions is very different from their behaviour under isolated discharge or charge processes, but surprisingly limited attention to this point has been devoted in the literature and recently our group decided to concentrate on this aspect (B. Bozzini et al., 2022b; Bozzini et al., 2020).

In this work, we focussed on quaternary ammonium salts (QAS) as prospective additives. Quaternary ammonium salts (QAS) are cationic surfactants, widely employed as additives in metal plating. They are stable in battery-relevant pH conditions. Under high cathodic polarization they can degrade through an irreversible reduction reaction, producing an amine and a hydrocarbon (Ross et al., 1960). No information can be found in the literature about the electrochemical oxidation of these compounds. Their positive effect on electrodeposition quality is well known, but their working mechanisms are poorly understood. QASs tend to adsorb on the cathode, thus blocking tip growth (Bayaguud et al., 2020) and increasing nucleation rate (Bressan and Wiert, 1979). The effect of QASs on the growth morphology depends strongly on the nature of the moieties bonded to the quaternary nitrogen: in aliphatic QASs the chain length is the controlling factor (Mackinnon and Brannen, 1982; Lan et al., 2007) and aromatic groups delocalize the positive charge of the nitrogen, decreasing adsorption strength (Fanigliulo and Bozzini, 2002). In particular, we selected four QASs, exhibiting characteristic molecular differences in the factors that dictate the interaction with

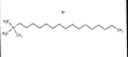
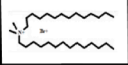
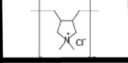

electrode surfaces in anodic and cathodic conditions, and interaction with the electrolyte,  $Zn^{2+}$ -species in particular (see Table 1). As far as QASs with long aliphatic chains are concerned, we selected: hexadecyl (or cetyl) tri-methyl ammonium bromide (CTAB) - a QAS surfactant with a single, 12 carbon atom-long aliphatic chain, commonly used in the metal-plating literature as a dendrite suppressor; and di-methyl di-tetradecyl ammonium bromide (DMDTDAB), with two 14 carbon atom-long aliphatic chain long aliphatic chains, tending to micellar formation (Yassine et al., 2007). In the other cases we chose polymers: benzyl-phenyl modified polyethyleneimine (BPPEI) and poly di-allyl di-methyl ammonium chloride (PDADMAC). These polymers exhibit different spacings amongst QA sites, in turn yielding different conformations and anion-transport properties. BPPEI has been successfully used as dendrite suppressor Cu plating (Bozzini et al., 2007) and PDADMAC is a polymer in which the tetravalent nitrogen is included in a five-atoms ring, that was adopted for the synthesis of composite conversion cathodes for lithium-ion batteries (Seoka et al., 2022; Osada et al., 2016; Tour et al., 2016). More details on QAS selection for Zn-based batteries can be found in Bozzini et al. (2020). Of course, the focus in this particular work is modelling of the cycling response and we refrain from giving an in-depth account of electrochemical materials-science aspects of Zn electrode behaviour in weakly acidic electrolytes without and with addition of quaternary ammonium salt (QAS) additives: these can be found in Bozzini et al. (2023).

Galvanostatic discharge/charge (GDC) cycling measurements were carried out in CR2032 coin cells, depicted in Fig. 5. The two electrodes were 12 mm diameter Zn disks (99.98% Alfa Aesar), 250  $\mu\text{m}$  in thickness. The Zn disks were contacted with stainless steel (AISI 304, diameter 12 mm, thickness 150  $\mu\text{m}$ ) and kept separated with a 260  $\mu\text{m}$  thick glass microfiber disk (Whatman), 19 mm in diameter, soaked with 350  $\mu\text{l}$  of 2 M  $ZnSO_4$  weakly acidic aqueous electrolyte, without and with added QAS (0.1  $\text{g l}^{-1}$  of CTAB, DMDTDAB and PDADMAC, 0.01  $\text{g l}^{-1}$  of BPPEI). GDC cycles were run at 1 and 10  $\text{mA cm}^{-2}$  with 60 min periods, corresponding to capacities of 0.5 and 5  $\text{mAh cm}^{-2}$ , respectively: we selected these values to be in line with the literature on GDC of ZIBs (see detailed discussion on this point in B. Bozzini et al. (2022b)), but it is worth noting that this is lower than that of practical battery operation (Parker et al., 2018). The experiments were terminated when the cell reached either short circuit (cell potential tending to zero) or passivation (absolute value of cell potential increasing beyond 1 V) conditions.

In Figs 6 we show the whole set of replicated cycling experiments, performed carried out at 1 and 10  $\text{mA cm}^{-2}$ . The time-to-failure for the

**Table 1**

Overview of the key outcomes of electrochemical measurements carried out in CR2032 coin cells with 2 M  $ZnSO_4$  weakly acidic aqueous electrolyte with the QAS additives indicated. (columns 1–5) time-to-failure for the two investigated current densities (columns 1 and 2), mean and standard deviation of cell voltage at steady-state (column 3), type sequence types, organized according to the parameter classification proposed (columns 4 and 5, see text for details) and SEM morphology observations (type of crystallite, column 6, and number density of crystallites, column 7).

		time to failure (h) 1 $\text{mA cm}^{-2}$	time to failure (h) 10 $\text{mA cm}^{-2}$	cell voltage @st.st / mV @1&10 $\text{mA cm}^{-2}$	sequence types 1 $\text{mA cm}^{-2}$	sequence types 10 $\text{mA cm}^{-2}$	SEM morphology @1 $\text{mA cm}^{-2}$	crystallite # density $10^{-3} \text{mm}^{-2}$
	no addit.	61.6±3.5	158±12	1: 35.6±9.0 10: 56.7±9.1	#1	#1	mossy	0.05042 ±0.01681
	CTAB	22.2±3.9	89.6±16.7	1: 69.7±14.5 10: –	#2	#3	globular	0.61345 ±0.10924
	DMDTDAB	30.3±1.0	1.1±0.4	1: 46.2±11.6 10: –	#2	-	mossy	0.08123 ±0.01284
	PDADMAC	23.5±3.5	16.5±7.8	1: 49.4±14.4 10: 54.9±9.4	#1	#1	globular	1.22409 ±0.16084
	BPPEI	43.0±8.5	17.0±8.5	1: 38.0±11.3 10: 40.1±8.1	#2⇒#1	#1	mossy	0.36975 ±0.20168

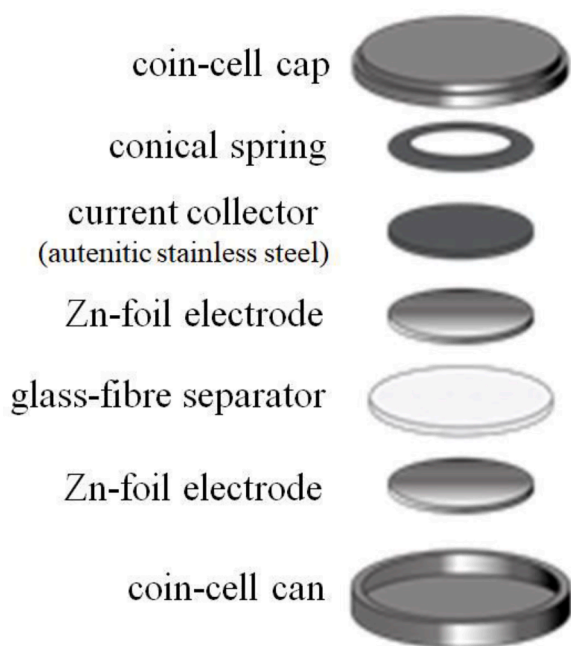


Fig. 5. Schematic of the assembly of the CR2032 coin cells used for galvanostatic cycling tests.

four systems are reported in the first two columns of Table 1. At these two c.d.s, of practical interest and corresponding to the mossy-growth range, the behaviour of Zn anodes is strongly impacted by the nature of the QAS, both positively and adversely, with respect to the additive-free case. Except with DMDTDAB, operation at the higher c.d. results in delayed failure. In addition, at  $1 \text{ mA cm}^{-2}$  all cells fail by short-circuit, while at  $10 \text{ mA cm}^{-2}$  short-circuit is the cause of termination with the polymeric QASs, and passivation in the absence of additives and with CTAB. Longer times-to-failure at higher c.d. can be explained with the fact that at low c.d.s the mossy Zn growth prevails and it is progressively reduced upon increasing the c.d. to an additive-dependent threshold for mossy growth suppression above  $20 \text{ mA cm}^{-2}$  (Bozzini et al., 2023). In a mossy-growth inhibition regime, passivation becomes to failure mode for the additive-free and CTAB-containing systems. Early failure by short circuit with DMDTDAB might be due to a lowering of the threshold c.d. for dendrite development, as suggested also by SEM imaging (Fig. 7).

Direct insight into Zn electrode shape changes can be obtained by *post mortem* imaging of Zn electrodes, extracted from cycled cells. For ease of electrode extraction, we employed an EL-CELL ECC-AIR-NI a split-cell, reproducing the geometry of 2032 coin cells. In the split-cell, the electrodes were kept separated by an O-ring and  $300 \mu\text{l}$  of free electrolyte were employed. Of course, testing with or without a separator, in principle, can yields different outcomes: to the best of the Authors' knowledge, this point has not been investigated so far, but this approach is appropriate for a ranking of the morphological impact of the different additives. After cycling for 14 h at  $1 \text{ mA cm}^{-2}$  - the more severe mossy growth condition -, the cells were disassembled and the Zn electrodes were rinsed with DI water and dried under  $\text{N}_2$  flow. The SEM micrographs are shown in Fig. 7. All images show a mixture of globular or filamentary Zn crystallites, resulting from the charging periods and ZnO platelets - covering the electrodeposited features - forming in the discharge intervals. Mossy structures dominate the additive-free and the BPPEI- and DMDTDAC-containing systems, while mossy growth suppression, witnessed by the formation of globular structures, is found with CTAB and PDMDMAC. Mossy growth suppression tendency correlates with higher crystallite density.

This complex scenario shows that the study of additives is strongly system-dependent, it requires specific fundamental understanding, and

performance indicators cannot be extrapolated from one system or operating condition to another one. The empirical understanding allowed by time-to-failure ranking and observation of the types of shape changes is indeed useful for electrolyte development, but hardly enables a knowledge-driven approach. Instead, analysis of the cycling time series, based in the model proposed in Section 2, allows to extract mechanistic information regarding the electrocrystallization processes occurring in the coin cells, that, in principle, can be plugged into further a predictive model of morphochemical metal evolution, such as the DIB model (Lacitignola et al., 2015; Lacitignola et al., 2014; Bozzini et al., 2013). Specifically, as detailed in Section 4, it is possible to assign metal growth, passivation and mass-transport parameters by comparing the experimental and computed potential responses to GDC cycling.

#### 4. Parameter classification

Parametric analysis of experimental cell-potential time-series has been carried out with the model proposed in Section 2. A definitive parameter identification task is beyond the scope of the present paper, and can be carried out with advanced NLLS approaches (Sgura et al., 2019) or with deep learning-based techniques (Sgura et al., 2023). In this context, a simple, but effective approach was that of classifying the experimental data in terms of the key parameter subspace, based on the principal analytical characteristics of the solutions of the model. In this way, we could frame in a clear-cut way the impact of electrolyte type and cycling c.d. on the cell response, in terms of materials properties, metal-electrode evolution modes, in particular.

Figure 8 report extracts of Fig. 6 that highlight the classes of charge-discharge switching transients found within the experimental corpus of this study.

Table 1 summarizes the key outcomes of electrochemical measurements (columns 1–5) and morphology observations by SEM (columns 6 and 7). Specifically, we report: the time to failure under GDC cycling at the two investigated current densities (columns 1 and 2), the cell voltage (average and standard deviation) measured after the cycling response attained steady-state conditions (column 3), the types of sequences of galvanostatic switching forms (columns 4 and 5), the type of surface morphology (column 6) and the number density of crystallites (column 7). The following key correlations can be noted. At  $1 \text{ mA cm}^{-2}$ , all additives increase the cell voltages with respect to the additive-free case, but the scenario is more complex at  $10 \text{ mA cm}^{-2}$ , were lower cell voltages correspond to passivation suppression. Globular morphology correlates with higher cell voltages, possibly owing to prevalence of the tip-inhibition mechanism (Bozzini et al., 2012). Type-1 sequences correspond to more stable electrode behaviour: the correlation with the time-to-failure and electrode morphology is more complex and will be commented in detail below. The type-2 sequence, instead, correlates with instability at higher current densities.

All the transients, their evolutions occurring during cycling and the corresponding simulations obtained with the model, can be represented in terms of three basic types of sequences, corresponding to systematic parameter variations, depicted in Panels A-C of Fig. 8. Type-1 sequence (Panel A) - that is the only pattern found with the additive-free and PDADMAC-containing electrolytes, both at a 1 and  $10 \text{ mA cm}^{-2}$  (Panels D-I, N, O), as well as of the BPPEI additive at  $10 \text{ mA cm}^{-2}$  (Panel S) - corresponds to a progressive increase of the effective diffusion coefficient, *ceteris paribus*. This sequence can be interpreted in terms of a progressive change from planar to spherical diffusion, associated with the formation of either mossy or globular growth features (see Fig. 7 and Table 1, column 6). Moreover, this kind of shape change is coherent with the initial decrease of the modulus of the cell voltage, that can be modelled with a finite value of the  $F_C$  parameter. The differences in cell lifetimes found for systems exhibiting type-1 sequences can be understood in terms of the fact that short circuits - especially of the transient type commonly found in these experiments - can result from the formation of progressive amounts of dead metal, eventually reaching the



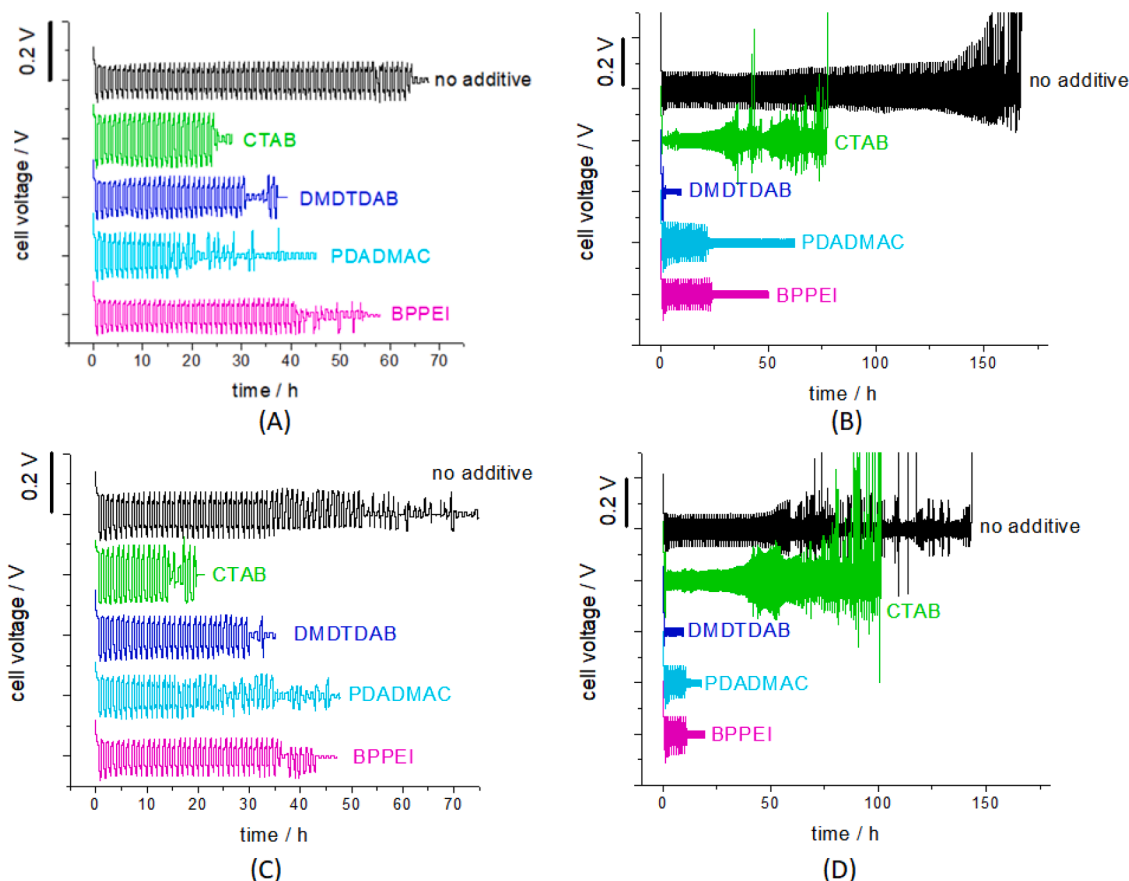


Fig. 6. Replicated galvanostatic cycling of Zn|Zn symmetric CR2023 coin cells with 2 M  $\text{ZnSO}_4$  electrolyte, with the indicated QASs. (A) and (C)  $1 \text{ mA cm}^{-2}$ ; (B) and (D)  $10 \text{ mA cm}^{-2}$ .

electronic percolation limit, that – if the average electrode area does not vary appreciably in time – would not yield a specific cell voltage response. This observation indicates an intrinsic limitation of lifetime diagnostic based solely on electrical cell responses, even of dynamic type, and calls for advanced monitoring approaches that can transduce to the battery management system, observables beyond electric ones. Nevertheless, approach to the percolation limit turns the electrolyte into an effectively porous one: this can explain the fact that, in the period before the short-circuit, the cell-voltage transient shape tends to go back to the type characteristic of a low  $D_{\text{eff}}$ .

The type-2 sequence (Panel B of Fig. 8) - observed at  $1 \text{ mA cm}^{-2}$  in the experiments with CTAB, DMDTDAB (Panels J and L) and the beginning of the experiments with BPPEI (Panels P and Q) – are characteristic of a condition whereby the cathodic kinetics is progressively enhanced, while the anodic one is inhibited. This kind of behaviour can be interpreted with the formation of a solid electrolyte interphase (SEI) layer, favoured by polymeric nature of additive, as observed with a different electrochemical approach in alkaline ambient (Bozzini et al., 2020). The change to type-1 sequence for BPPEI after ca. 5 h of cycling (Panel P) indicates the stabilization of an outgrowth morphology with well-adhered crystallites. The transient short circuit events, that can be observed in this case (Panel R), confirm this explanation. Cell termination by short-circuit at  $10 \text{ mA cm}^{-2}$  with BPPEI (Panel S), instead of the passivation-driven end-of-life found in the additive-free case, might be related to the fact that SEI formation prevents passivation.

The CTAB-containing cell at  $10 \text{ mA cm}^{-2}$  (Panel K) is the only occurrence of the type-3 sequence (Panel C) in this research. This sequence is characteristic of high  $\text{Zn}^{2+}$  concentrations in the electrolyte, combined with a high  $D_{\text{eff}}$ . Experimentally, this peculiar dynamic behaviour correlates with a tendency to transient passivation and cell

failure by passivation, a relatively long cell lifetime and the stabilization of a globular morphology. These processes and the corresponding parameter values, correlate clearly with the high cathodic inhibition afforded by CTAB (Bozzini et al., 2023) causing, on the one hand, an accumulation of corrosion products, and, on the other hand catholyte alcalinization with attending zincate formation and final ZnO precipitation (Kazemian et al., 2022; Bozzini et al., 2022a), all these processes are passivation precursors.

## 5. Conclusions

The shape stability of metallic anodes during discharge-charge cycles is a crucial requirement for the practical deployment of next-generation high energy-density batteries. Symmetric-cell testing is a simple, but efficient approach for bridging the gap between advances at material-science level and operation of practical devices. Currently, the generation of high-quality experimental data and theoretical tools to exploit them to gain insight into material evolution inside the cell are not much developed. This paper proposes a combined theoretical-experimental approach to tackle this challenge. In particular, we have carried out a systematic analysis of the galvanostatic cycling – under practically relevant operating conditions – of Zn symmetrical 2032-type coin-cells with weakly acidic electrolyte, containing a range of quaternary ammonium salt (QAS) additives, meant to promote anode shape stability.

Some QASs with a simpler molecular structure (CTAB, PDADMAC), resulting in higher surface coverages during the cathodic cycle, can improve metal shape – in correspondence to an increase of nucleation rate and cell overvoltage –, but this improvement is not related to an increase of cell lifetime, that in weakly acidic electrolytes – at variance

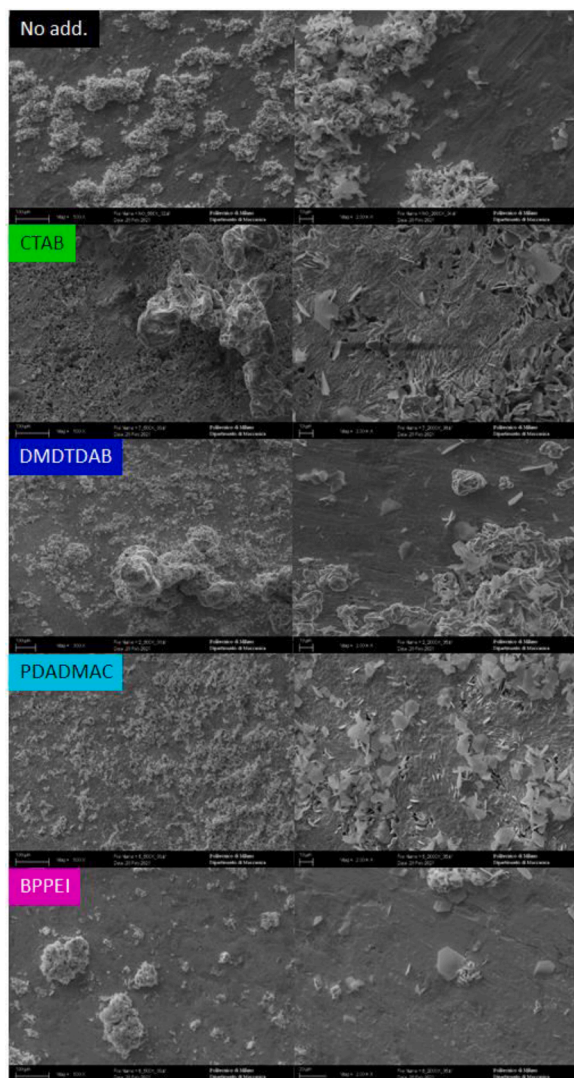


Fig. 7. SEM micrographs of Zn electrodes cycled galvanostatically at  $1 \text{ mA cm}^{-2}$  in a split-cell, with  $2 \text{ M ZnSO}_4$  electrolyte, containing the indicated QASs.

with alkaline systems – seems to be better in the absence of the additives considered. Moreover, polymeric QASs (PDADMAC, BPPEI) give the same dynamic cell voltage response as the additive-free case, but cell lifetime is adversely affected, notwithstanding the suppression of passivation through a reduction of the amount of Zn corrosion products in the electrolyte.

Systematic study of QASs thus discloses a scenario of additive impact, that is notably more complex than what one might conclude from the literature. In fact, available publications mostly consider individual additives, anodic or cathodic processes in insulation and a

limited range of operating conditions. Systematic investigation, and the necessity of obtaining a firm knowledge base in the field, call for a solid theoretical framework, that can be readily employed as a tool for data elaboration.

The model we are proposing in this work copes with this issue, enabling a link between the electrical cell response and cell material evolution. This approach opens up the possibility of following hidden variables correlating electrical operating parameters (c.d.) response (cell voltage) and quantities describing cell material dynamics: transient and cumulative electrode shape changes, electrode passivation, electrolyte chemistry, accumulation of dead metal. All these aspects contribute to cell failure and determine specific failure modes, though through different evolution pathways, that have to be understood in order to counteract them effectively, either by material optimization or by improved battery management protocols.

The observed cell voltage time series can be described in terms of the proposed mathematical model. This allows a more insightful exploitation of the results of other complementary measurements, such as microimaging of the electrode, considered in this work. Classification of chronopotentiometric transients, in dependence of specific variations of some parameters, allows better understanding of the key processes occurring in the cell and of their concrete impact on device durability, that was, in some cases, found to be counterintuitive.

Future developments of this approach will allow to proceed beyond the efficient, but semi-quantitative parameter classification approach, reaching a full quantification thanks to fast and reliable parameter identification. In *Sgura et al. (2023)* we have shown that parameter identification tasks for PDE models and complex experimental datasets can be effectively carried out with deep-learning (DL) methods, and this approach will be implemented for the model described in this work. In particular, a major step forward enabled by DL would be a systematic and comprehensive exploration of the parameter space, along three key directions. (i) In-depth exploration of the currently better-known section of the parameter space, that gave rise to the three sequence types that can follow the experimental datasets of this research: the outcome will be the automatic partitioning of the model solutions into zones in which specific types of cycling response prevail. (ii) Extension of the classification of solutions to the full parameter space. (iii) Parameter identification, allowing to assigning sets of model parameters to experimental time series. In its maturity, this approach – ideally in combination with the transduction of material-relevant quantities to the BMS, will enable control of batteries based on the precise knowledge of their status.

#### Declaration of Competing Interest

The authors declare that they have no known competing financial interests or personal relationships that could have appeared to influence the work reported in this paper.

#### Data availability

Data will be made available on request.

### Appendix 1. COMMENTS ON THE PARAMETERS CONTAINED IN THE MODEL (INCLUDING BOTH PDE MODEL AND THE CORRESPONDING BCs)

#### 2.3.1) Comments on the parameter space of the BC model

The BC model, contains the parameters classified and discussed below. Overall, once the type of electrodic metal is selected, fixing 4 “constant material parameters” (b1-b4), and the experimental conditions are set by fixing 3 “operating parameters” (a1-a3), the performance of the material can be followed by identifying 8 “variable materials parameters (c1-c8).

a) Operating parameters: these parameters correspond to the imposed operating conditions of the cell. In a given experiment, they can be regarded as constant.

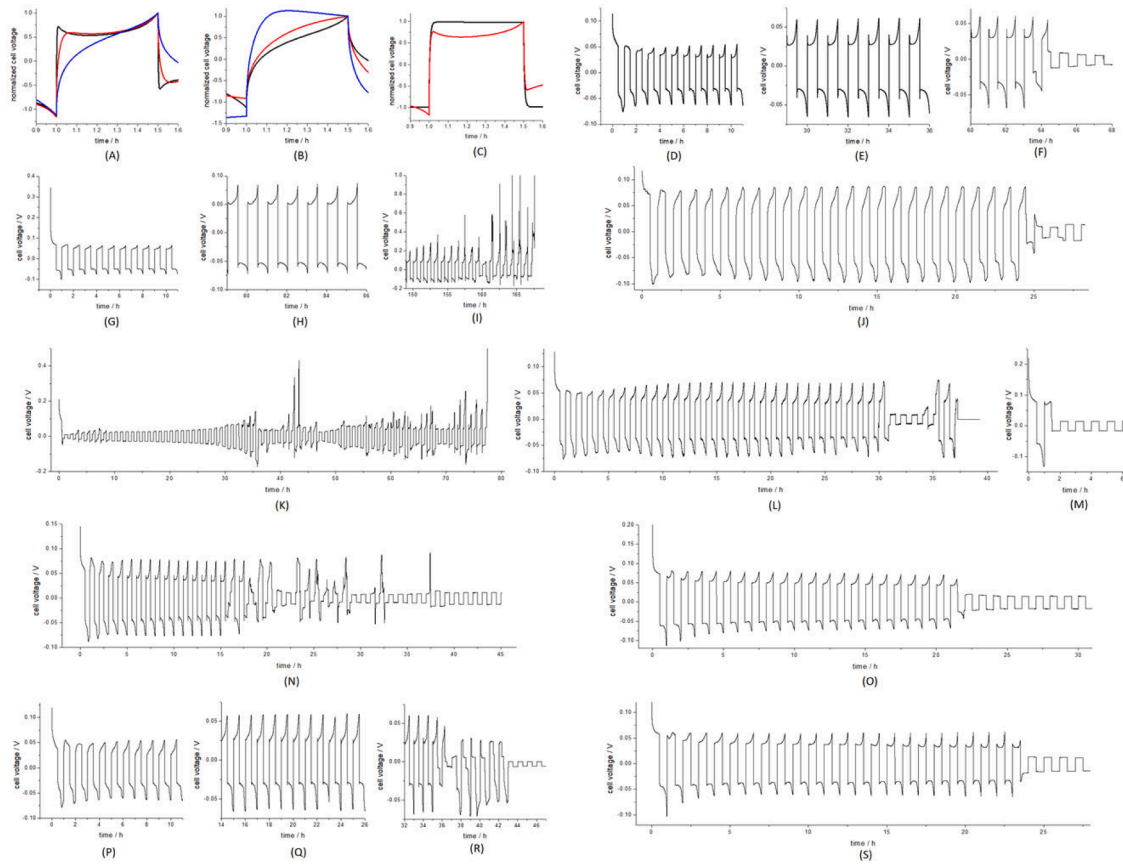


**Fig. 8.** Types of cell voltage transients, computed (A-C) and experimental (D-S), resulting from the application of GDC cycles. (A) Computed sequence type #1 -  $D = 1e^{-4}$  (black),  $1e^{-5}$  (red),  $1e^{-6}$  (blue)  $\text{cm}^2 \text{s}^{-1}$ . Common parameters:  $i = 50 \text{ mA cm}^{-2}$ ,  $[\text{Zn}^{2+}] = 50 \text{ mM}$ ,  $k_{o,hs} = 7e^{-6} \text{ cm s}^{-1}$ ;  $k_{o,flat} = 9e^{-8} \text{ cm s}^{-1}$ ,  $\kappa = 2e^{-3} [\Omega^{-1} \text{ cm}^{-1}]$ . (B) Computed sequence type #2 - black plot:  $i = 50 \text{ mA cm}^{-2}$ ,  $k_{o,hs} = 7e^{-6} \text{ cm s}^{-1}$ ,  $k_{o,flat} = 9e^{-8} \text{ cm s}^{-1}$ ; red plot:  $i = 50 \text{ mA cm}^{-2}$ ,  $k_{o,hs} = 7e^{-6} \text{ cm s}^{-1}$ ,  $k_{o,flat} = 9e^{-5} \text{ cm s}^{-1}$ ; blue plot:  $i = 5 \text{ mA cm}^{-2}$ ,  $k_{o,hs} = 3.5e^{-6} \text{ cm s}^{-1}$ ,  $k_{o,flat} = 9e^{-7} \text{ cm s}^{-1}$ . Common parameters:  $D = 1e^{-6} \text{ cm}^2 \text{ s}^{-1}$ ;  $[\text{Zn}^{2+}] = 50 \text{ mM}$ ;  $\kappa = 2e^{-3} [\Omega^{-1} \text{ cm}^{-1}]$ . (C) Computed sequence type #3 - black plot:  $k_{o,hs} = 1e^{-6} \text{ cm s}^{-1}$ ,  $k_{o,flat} = 9e^{-7} \text{ cm s}^{-1}$ ; red plot:  $k_{o,hs} = 3.5e^{-6} \text{ cm s}^{-1}$ . Common parameters:  $D = 3.6e^{-5} \text{ cm}^2 \text{ s}^{-1}$ ,  $i = 5 \text{ mA cm}^{-2}$ ,  $[\text{Zn}^{2+}] = 50 \text{ mM}$ ,  $\kappa = 2e^{-3} [\Omega^{-1} \text{ cm}^{-1}]$ . No additive: 1 (D-F), 10 (G-I)  $\text{mA cm}^{-2}$ . CTAB: 1 (J), 10 (K)  $\text{mA cm}^{-2}$ . DMDTDAB: 1 (L), 10 (M)  $\text{mA cm}^{-2}$ . PDADMAC: 1 (N), 10 (O)  $\text{mA cm}^{-2}$ . BPPEI: 1 (P-R), 10 (S)  $\text{mA cm}^{-2}$ .

- a1)  $I [\text{A cm}^{-2}]$  of Eq. (1), the imposed c.d.
- a2)  $T [\text{s}]$  of Eq. (2), the duration of the current cycle (positive/negative current cycle).
- a3) Number of cycles: the total time  $t_{\text{tot}}$  implicitly considered in the model is in fact  $t_{\text{tot}} = T \cdot N$ .

b) Constant material parameters: these parameters either depend on the material properties, but are known a priori or are physical constants.

- e1) The atomic weight  $[\text{g mol}^{-1}]$ , implicitly considered in Eq. (13).
- e2)  $\rho [\text{g cm}^{-3}]$  the density of Eq. (13).
- e3)  $z [\text{eq mol}^{-1}]$  the valency of Eq. (1).
- e4)  $F [\text{C eq}^{-1}]$  the Faraday constant of Eq. (1).

c) Variable material parameters: these parameters depend on the material properties. These parameters have to be identified from an experiment, if this is meant to qualify the material behaviour.

- c1)  $F_C [1]$  of Eq. (8a,b,c), the propensity to outgrowth of the metal in context.
- c2)  $r_{\text{max}} [\text{cm}]$  of Eq. (6), a quantity describing the areal number density of electrodeposited nuclei (the higher  $r_{\text{max}}$ , the lower the density of nuclei).
- c3)  $k_{hs,pass} [1]$  of Eq. (9a), a quantity describing the propensity to passivation of the outgrowth features, for the lower electrode (in which passivation is favoured by gravitational effects).
- c4)  $k_{hs,flat} [1]$  of Eq. (9b), a quantity describing the propensity to passivation of the electrode in the regions in which outgrowth features are not present, for the lower electrode (in which passivation is favoured by gravitational effects).
- c5)  $k_{hs,pass}^{\text{upper}} [1]$  of Section 2.2.1, a quantity describing the propensity to passivation of the outgrowth features, for the upper electrode (in which passivation is not favoured by gravitational effects).
- c6)  $k_{hs,flat}^{\text{upper}} [1]$  of Section 2.2.1, a quantity describing the propensity to passivation of the electrode in the regions in which outgrowth features are not present, for the upper electrode (in which passivation is not favoured by gravitational effects).
- c7)  $k_{o,hs} [\text{cm s}^{-1}]$  of Eq. (10), the electrodeposition kinetic constant in correspondence of the outgrowth features.

c8)  $k_{o,flat}$  [ $\text{cm s}^{-1}$ ] of Eq. (10), the electrodeposition kinetic constant in correspondence of the electrode in the regions in which outgrowth features are not present.

Physically reasonable values of  $k_o$  are discussed below. (i) With  $\beta=0.5$  and  $\eta=0.1$  V,  $\exp(\pm\beta\cdot F\cdot\eta/8.31/300)=0.1\div 10$ . (ii)  $c\sim 1e^{-3}\div 1$  M. (iii)  $\gamma\sim 1\div 10$ . (iv)  $i\sim 1e^{-3}$  A  $\text{cm}^{-2}$ . Considering all maximum values and all minimum values:  $k_o\sim 1e^{-4}\div 1e^{-10}$ .

It is worth noting that, according to Eq. (19), the quantity actually controlling the time-dependence of the electrode area is the ratio of  $k_{o,hs}$  and  $k_{o,flat}$ , this ratio can thus be regarded as the a single independent variable in the parametric analysis of the model.

The “variable material parameters” can be further classified according to the underlying physics, as follows:

- kinetic parameters describing electrokinetics of electrodeposition (c7, c8);
- geometrical parameters describing: nucleation (c2) and unstable outgrowth (dendrite formation, c1);
- kinetic parameters describing passivation (c3-c6).

### 2.3.2) Comments on the parameter space of the PDE model

The PDE model, contains the parameters classified and discussed below. Overall, once the type of metal is selected, fixing 3 “constant material parameters” (f1-f3), and the experimental conditions are set by fixing 2 “operating parameters” (e1-e3), the cell dynamics should be followed by adjusting the 4 “variable materials parameters” (g1-g4).

e) Operating parameters:

e1) L [cm], defining the integration domain.

e2)  $t_{exp}$  [s] has the same meaning as  $t_{tot}$  defined in points (a2) and (a3) above.

f) Constant material parameters: see point (b) in Section 1. F (Eq. (11)) and z (Eq. (11)) are commented there.

f1) R [ $\text{C V T}^{-1} \text{mol}^{-1}$ ] of Eq. (11) is the gas constant: a physical constant.

f2)  $u_o$  [ $\text{mol cm}^{-3}$ ] of Eq. (17a,b) is the initial concentration of the electroactive species.

f3) A [ $\text{cm}^2$ ] of Eq. (19) is the area of the electrode, this quantity is implicitly included in the numerical value of I (a1).

g) Variable material parameters:

The variable material parameters mentioned in this subsection depend on the details of the electrolyte composition (that is modelled in this context in terms of  $u$ ) and of the surface condition of the metal (that is related to the parameters (c3)-(c7)). For first-approximation work, they can be regarded as constants.

g1) D [ $\text{cm}^2 \text{s}^{-1}$ ] of Eq. (11) is the diffusion coefficient, in fact this depends on the electrolyte composition.

g2)  $\kappa$  [ $\Omega^{-1} \text{cm}$ ] of Eq. (21) is the electrolyte conductivity. Its value depends on the electrolyte concentration and in principle can also be modelled as a function of D.

g3) B [V] of Eq. (22) electrokinetic parameter of the electrodeposition reaction. Its value depends on the specific reaction and in principle depends on the evolution of the system chemistry and is correlated with parameters (c7-c8).

g4)  $i_o$  [ $\text{A cm}^{-2}$ ] of Eq. (22) another electrokinetic parameter, same comments apply as to point (f6).

## Appendix 2. MATLAB formalism for PDEPE solver

The system Eq.s (12) and (13) with BCs Eq.s 17–(19) and ICs Eq.s (20), can be conveniently integrated with the PDEPE MATLAB solver. For the readers’ perusal, as well as for the sake of often neglected transparency, we recast the problem defined in Sections (2.2.1–2.2.4) in the PDEPE formalism.

PDEPE solves systems of 1D in space elliptic and parabolic PDEs of the following form:

$$\bar{c}\left(x, t, \bar{v}, \frac{\partial \bar{v}}{\partial x}\right) \cdot \frac{\partial \bar{v}}{\partial t} = x^{-m} \frac{\partial}{\partial x} \left[ x^m \bar{f}\left(x, t, \bar{v}, \frac{\partial \bar{v}}{\partial x}\right) \right] + s\left(x, t, \bar{v}, \frac{\partial \bar{v}}{\partial x}\right) \quad (\text{A1})$$

where a bar above a symbol denotes its vectorial nature and  $\cdot$  indicates the scalar product.

Inspection shows that setting  $m = 0$ ,  $s=0$  the structure of system Eq.s (12), (13) is obtained, with the following definitions:

$$\bar{v} = \begin{pmatrix} \phi \\ u \end{pmatrix}, \quad \bar{c} = \begin{pmatrix} 0 \\ 1 \end{pmatrix}, \quad \bar{f} = \begin{pmatrix} \frac{\partial \phi}{\partial x} \\ -J \end{pmatrix} \quad (\text{A2})$$

In PDEPE the BCs are expressed in the form:

$$\bar{p}[x=0, t, \bar{v}(x=0, t)] + \bar{q}(x=0, t) \cdot \bar{f}\left(x=0, t, \bar{v}, \frac{\partial \bar{v}}{\partial x}\right)_{x=0,t} = 0 \quad (\text{A3a})$$



$$\bar{p}[x=L, t, \bar{v}(x=L, t)] + \bar{q}(x=L, t) \cdot \bar{f}\left(x=L, t, \bar{v}, \frac{\partial \bar{v}}{\partial x}\bigg|_{x=L, t}\right) = 0 \quad (\text{A3b})$$

Inserting Eq.s (17), (18) into Eq. (A3), one gets:

$$\bar{p}[x=0, t, \bar{v}(x=0, t)] = \left( \begin{array}{c} \phi(x=0, t) - \frac{RT}{zF} \ln \left[ \frac{u(x=0, t)}{u_o} \right] \\ \frac{I(t)}{A \cdot k_o(t)} \end{array} \right) \quad (\text{A4a})$$

$$\bar{p}[x=L, t, \bar{v}(x=L, t)] = \left( \begin{array}{c} \phi(x=L, t) - \frac{RT}{zF} \ln \left[ \frac{u(x=L, t)}{u_o} \right] \\ \frac{I(t)}{A \cdot k_o(t - T/2)} \end{array} \right) \quad \text{where } k_o(\tau) = 1 \text{ for } \tau \leq 0 \quad (\text{A4b})$$

$$\bar{q}(x=0, t) = \bar{q}(x=L, t) = \begin{pmatrix} 0 \\ 1 \end{pmatrix} \quad (\text{A4c})$$

$$\bar{f}\left(x=0, t, \bar{v}, \frac{\partial \bar{v}}{\partial x}\bigg|_{x=0, t}\right) = \left( \begin{array}{c} \frac{\partial \phi}{\partial x}\bigg|_{x=0, t} \\ \frac{I(t)}{zFA \cdot k_o(t)} \end{array} \right) \quad (\text{A4d})$$

$$\bar{f}\left(x=L, t, \bar{v}, \frac{\partial \bar{v}}{\partial x}\bigg|_{x=L, t}\right) = \left( \begin{array}{c} \frac{\partial \phi}{\partial x}\bigg|_{x=L, t} \\ \frac{I(t)}{zFA \cdot k_o(t)} \end{array} \right) \quad (\text{A4e})$$

No special comments are required for the ICs.

## References

- An, Q., Luo, P., Xiao, Y., Yang, J., Zuo, C., Xiong, F., Tang, C., Liu, G., Zhang, W., Tang, W., Wang, S., Dong, S., 2022. Polyaniline nanoarrays/carbon cloth as binder-free and flexible cathode for magnesium ion batteries. *J. Chem. Eng.* v433 <https://doi.org/10.1016/j.cjce.2021.133772>.
- Bayaguud, A., Luo, X., Fu, Y., Zhu, C., 2020. Cationic surfactant-type electrolyte additive enables three-dimensional dendrite-free zinc anode for stable zinc-ion batteries. *ACS Energy Lett* v5. <https://doi.org/10.1021/acsenenergylett.0c01792>.
- Bozzini, B., Boniardi, M., Caielli, T., Casaroli, A., Emanuele, E., Mancini, L., Sodini, N., Strada, J., 2023. Electrochemical cycling behaviour and shape changes of Zn electrodes in mildly acidic aqueous electrolytes containing quaternary ammonium salts. *ChemElectroChem*.
- Bozzini, B., D'Urzo, L., Mele, C., 2007. A novel polymeric leveller for the electrodeposition of copper from acidic sulphate bath: a spectroelectrochemical investigation. *Electrochim. Acta* v52. <https://doi.org/10.1016/j.electacta.2007.01.015>.
- Bozzini, B., Lactignola, D., Mele, C., Sgura, I., 2012. Morphogenesis in metal electrodeposition. *Note di Mat.* v32 <https://doi.org/10.1285/i15900932v32n1p7>.
- Bozzini, B., Lactignola, D., Sgura, I., 2013. Spatio-temporal organisation in alloy electrodeposition: a morphochemical mathematical model and its experimental validation. *J. Solid State Electrochem.* v17 <https://doi.org/10.1007/s10008-012-1945-7>.
- Bozzini, B., Amati, M., Gregoratti, L., Lactignola, D., Sgura, I., Krastev, I., Drobovolska, T., 2015. Intermetallics as key to spiral formation in In-Co electrodeposition. A study based on photoelectron microspectroscopy, mathematical modelling and numerical approximations. *J. Phys. D* v48. <https://doi.org/10.1088/0022-3727/48/39/395502>.
- Bozzini, B., Rossi, F., Mele, C., Boniardi, M., 2020. Electrodeposition of Zn from alkaline electrolytes containing quaternary ammonium salts and ionomers: the impact of cathodic-anodic cycling conditions. *ChemElectroChem* v7. <https://doi.org/10.1002/celec.202000165>.
- Bozzini, B., Kazemian, M., Rossi, F., Casaroli, A., Caielli, T., Kaulich, B., Kiskinova, M., Sgura, I., 2022a. X-ray imaging and micro-spectroscopy unravel the role of zincate and zinc oxide in the cycling of zinc anodes in mildly acidic aqueous electrolytes. *J. Power Sources* v524. <https://doi.org/10.1016/j.jpowsour.2022.231063>.
- Bozzini, B., Rossi, F., Mancini, L., Sgura, I., Boniardi, M., Casaroli, A., Kao, A.P., 2022b. Insight into the cycling behaviour of metal anodes, enabled by X-ray tomography and mathematical modelling. *ChemElectroChem* v9. <https://doi.org/10.1002/celec.202101537>.
- Bozzini, B., Bagheri, S., Boniardi, M., Mancini, L., Marini, E., Sgura, I., Mele, C., 2022c. Quantifying and rationalizing polarization curves of Zn-air fuel-cells: a simple enabling contribution to device-scale analysis and monitoring. *Electrochim. Acta* v425. <https://doi.org/10.1016/j.electacta.2022.140712>.
- Bressan, J., Wiart, R., 1979. Inhibited zinc electrodeposition: electrode kinetics and deposit morphology. *J. Appl. Electrochem.* v9 <https://doi.org/10.1007/BF00620586>.
- Chazalviel, J.N., 1990. Electrochemical aspects of the generation of ramified metallic electrodeposits. *Phys. Rev. A* v42. <https://doi.org/10.1103/PhysRevA.42.7355>.
- Chen, C.P., Jorne, J., 1990. Fractal analysis of zinc electrodeposition. *J. Electrochem. Soc.* v137 <https://doi.org/10.1149/1.2086862>.
- Chen, W., Zheng, X., Ahmad, T., 2021. Challenges and strategies on Zn electrodeposition for stable Zn-ion batteries. *Energy Stor. Mater.* v39 <https://doi.org/10.1016/j.enstm.2021.04.027>.
- Dasgupta, N.P., Chen, K.-H., Wood, K.N., Kazyak, E., Page, W.S.L., Davis, A.L., Sanchez, A.J., 2017. Dead lithium: mass transport effects on voltage, capacity, and failure of lithium metal anodes. *J. Mater. Chem. A* v5. <https://doi.org/10.1039/C7TA00371D>.
- Desai, D., Turney, D.E., Anantharaman, B., Steingart, D.A., Banerjee, S., 2014. Morphological evolution of nanocluster aggregates and single crystals in alkaline zinc electrodeposition. *J. Phys. Chem. C*, v118. <https://doi.org/10.1021/jp411104a>.
- Diggle, J.W., Despic, A.R., Bockris, J., 1969. The Mechanism of the dendritic electrocrystallization of zinc. *J. Electrochem. Soc.* v116 <https://doi.org/10.1149/1.2411588>.
- Fanigliulo, A., Bozzini, B., 2002. An electrochemical and SERS study of benzyldimethylphenylammonium chloride at a polycrystalline gold electrode. *Electrochim. Acta*, v47. [https://doi.org/10.1016/S0013-4686\(02\)00538-8](https://doi.org/10.1016/S0013-4686(02)00538-8).
- Fletcher, S., 1983. Electrochemical deposition of hemispherical nuclei under diffusion control. Some theoretical considerations. *J. Chem. Soc., Faraday Trans.*, v79. <https://doi.org/10.1039/F19837900467>.
- Gallant, B.M., Guo, R., Hobold, G.M., 2022. The ionic interphases of the lithium anode in solid state batteries. *Curr. Opin. Solid State Mater. Sci.* v26 <https://doi.org/10.1016/j.cossms.2021.100973>.
- Hamilton, D.R., 1963. A theory of dendritic growth in electrolytes. *Electrochim. Acta* v8. [https://doi.org/10.1016/0013-4686\(63\)85018-5](https://doi.org/10.1016/0013-4686(63)85018-5).

- Han, Y., Liu, B., Xiao, Z., Zhang, W., Wang, X., Pan, G., Xia, Y., Xia, X., Tu, J., 2021. Interface issues of lithium metal anode for high-energy batteries: challenges, strategies, and perspectives. *InfoMat* v3. <https://doi.org/10.1002/inf2.12166>.
- Higashi, S., Lee, S.W., Lee, J.S., Takechi, K., Cui, Y., 2016. Avoiding short circuits from zinc metal dendrites in anode by backside-plating configuration. *Nat. Commun.* v7 <https://doi.org/10.1038/ncomms11801>.
- Kazemian, M., Rossi, F., Casaroli, A., Caielli, T., Kaulich, B., Kiskinova, M., Sgura, I., Bozzini, B., 2022. Soft-X ray absorption spectromicroscopy unravels the role of zincate and zinc oxide in the cycling of zinc anodes in mildly acidic aqueous electrolytes. *J. Power Sources* 524, 231063. <https://doi.org/10.1016/j.jpowsour.2022.231063>.
- Khewhom, S., Khezri, R., Motlagh, S., Etesami, M., Mohamad, A.A., Mahlendorf, F., Somwangthanaroj, A., 2022. Stabilizing zinc anodes for different configurations of rechargeable zinc-air batteries. *J. Chem. Eng.* v449 <https://doi.org/10.1016/j.cej.2022.137796>.
- Lacitignola, D., Bozzini, B., Sgura, I., 2014. Spatio-temporal organization in a morphochemical electrodeposition model: analysis and numerical simulation of spiral waves. *Acta Appl. Math.* v132 <https://doi.org/10.1007/s10440-014-9910-3>.
- Lacitignola, D., Bozzini, B., Sgura, I., 2015. Spatio-temporal organization in a morphochemical electrodeposition model: hopf and turing instabilities and their interplay. *Eur. J. Appl. Math.* v26 <https://doi.org/10.1017/S0956792514000370>.
- Lan, C.J., Lee, C.Y., Chin, T.S., 2007. Tetra-alkyl ammonium hydroxides as inhibitors of Zn dendrite in Zn-based secondary batteries. *Electrochim. Acta*, v52. <https://doi.org/10.1016/j.electacta.2007.02.063>.
- Li, C.C., Du, W., Ang, E.H., Yang, Y., Zhang, Y., Ye, M., 2020. Challenges in the material and structural design of zinc anode towards high-performance aqueous zinc-ion batteries. *Energy Environ. Sci.* v13 <https://doi.org/10.1039/D0EE02079F>.
- Liang, J., Yi, Z., Chen, G., Hou, F., Wang, L., 2021. Strategies for the stabilization of Zn metal anodes for Zn-ion batteries. *Adv. Energy Mater.* V11 <https://doi.org/10.1002/aenm.202003065>.
- Ling, T., Jiao, D., Ma, Z., Li, J., Han, Y., Mao, J., Qiao, S., 2020. Test factors affecting the performance of zinc-air battery. *J. Energy Chem.* v44 <https://doi.org/10.1016/j.ijechem.2019.09.008>.
- Liu, T.L., Wei, Q., Zhang, L., Sun, X., 2022. Progress and prospects of electrolyte chemistry of calcium batteries. *Chem. Sci.* v13 <https://doi.org/10.1039/D2SC00267A>.
- Lu, Y., Tu, Z., Archer, L.A., 2014. Stable lithium electrodeposition in liquid and nanoporous solid electrolytes. *Nat. Mater.* v13 <https://doi.org/10.1038/NMAT4041>.
- Lucas, S., Moskovkin, P., 2010. Simulation at high temperature of atomic deposition, islands coalescence, ostwald and inverse ostwald ripening with a general simple kinetic Monte Carlo Code. *Thin Solid Films* v518. <https://doi.org/10.1016/j.tsf.2010.04.064>.
- Ma, J., Qi, S., Xu, B., Tiong, V.T., Hua, J., 2020. Progress on iron oxides and chalcogenides as anodes for sodium-ion batteries. *J. Chem. Eng.* v379 <https://doi.org/10.1016/j.cej.2019.122261>.
- Mackinnon, D.J., Brannen, J.M., 1982. Evaluation of organic additives as levelling agents for zinc electrowinning from chloride electrolytes. *J. Appl. Electrochem.* v12 <https://doi.org/10.1007/BF01112061>.
- Mai, L., Zhang, X., Xu, X., Song, B., Duan, M., Meng, J., Wang, X., Xiao, Z., Xu, L., 2022. Towards a stable layered vanadium oxide cathode for high-capacity calcium batteries. *Small.* <https://doi.org/10.1002/sml.202107174>.
- Minguzzi, A., Pargoletti, E., Arnaboldi, S., Cappelletti, G., Longhi, M., Meroni, D., Mussini, P.R., Rondinini, S., Vertova, A., 2022. Smart interfaces in Li-ion batteries: near-future key challenges. *Electrochim. Acta* v415. <https://doi.org/10.1016/j.electacta.2022.140258>.
- Osada, N., Bucur, C.B., Aso, H., Muldoon, J., 2016. The design of nanostructured sulfur cathodes using layer by layer assembly. *Energy Environ. Sci.* v9 <https://doi.org/10.1039/c6ee00444j>.
- Newman, J.S., 1991. *Electrochemical Systems*, 2nd ed. Prentice Hall Englewood N.J. Cliffs, pp. 16–18 (Chapters).
- Palacin, M.R., Ponrouch, A., 2019. Post-Li batteries: promises and challenges. *Phil. Trans. R. Soc. A* v377. <https://doi.org/10.1098/rsta.2018.0297>.
- Parker, J.F., Ko, J.S., Rolison, D.R., Long, J.W., 2018. Translating materials-level performance into device-relevant metrics for zinc-based batteries. *Joule* v2. <https://doi.org/10.1016/j.joule.2018.11.007>.
- Ponrouch, A., Dugas, R., Forero-Saboya, J.D., 2019. Methods and protocols for reliable electrochemical testing in post-Li batteries (Na, K, Mg, and Ca). *Chem. Mater.* v31 <https://doi.org/10.1021/acs.chemmater.9b02776>.
- Popov, K.I., Djokic, S.S., Grgur, B.N., 2002. *Fundamental aspects of electrometallurgy*. N. Y. Kluwer, (Chapters 3 and 5).
- Ross, S.D., Finkelstein, M., Petersen, R.C., 1960. The electrochemical degradation of quaternary ammonium salts. II. The mechanism of the coupling reaction. *J. Am. Chem. Soc.* v82 <https://doi.org/10.1021/ja01492a017>.
- Seoka, E., Kim, M., Lee, S., Park, J., Ku, M., Lim, H., Lee, Y., Yu, S., Choi, W., 2022. Electrostatic interaction-driven inorganic coating layer toward improving battery performance for 5V class high-voltage. SSRN. <https://ssrn.com/abstract=4161664>.
- Sgura, I., Lawless, A.S., Bozzini, B., 2019. Parameter estimation for a morphochemical reaction-diffusion model of electrochemical pattern formation. *Inverse Probl. Sci. Eng.* v27 <https://doi.org/10.1080/17415977.2018.1490278>.
- Sgura, I., Mainetti, L., Negro, F., Quarta, M.G., Bozzini, B., 2023. Deep-learning based parameter identification enables rationalization of battery material evolution in complex electrochemical systems. *J. Comput. Sci.* 66, 101900 <https://doi.org/10.1016/j.jocs.2022.101900>.
- Sluyters, J.H., Sluyters-Rehbach, M., Wijenberg, J.H.O.J., Bosco, E., 1987. The theory of chronoamperometry for the investigation of electrocrystallization: mathematical description and analysis in the case of diffusion-controlled growth. *J. Electroanal. Chem.* v236 [https://doi.org/10.1016/0022-0728\(87\)88014-2](https://doi.org/10.1016/0022-0728(87)88014-2).
- Stucky, G.D., Li, X., Sun, X., Hu, X., Fan, F., Cai, S., Zheng, C., 2020. Review on comprehending and enhancing the initial Coulombic efficiency of anode materials in lithium-ion/sodium-ion batteries. *Nano Energy* v77. <https://doi.org/10.1016/j.nanoen.2020.105143>.
- Sun, Y., Lei, L., Wang, X., Jiang, Y., Li, J., 2020. Strategies to enhance corrosion resistance of Zn electrodes for next generation batteries. *Front. Mater.* v7 <https://doi.org/10.3389/fmats.2020.00096>.
- Sun, Y., Ou, Y., Cai, Z., Wang, J., Zhan, R., Liu, S., Lu, Z., 2022. Reversible aqueous Zn battery anode enabled by a stable complexation adsorbent interface. *EcoMat* v4. <https://doi.org/10.1002/eom2.12167>.
- Tour, J.M., Li, L., Gao, C., Kovalchuk, A., Peng, Z., Ruan, G., Yang, Y., Fei, H., Zhong, Q., Li, Y., 2016. Sandwich structured graphene-wrapped FeS-graphene nanoribbons with improved cycling stability for lithium ion batteries. *Nano Res* v9. <https://doi.org/10.1007/s12274-016-1175-x>.
- Wang, K., Pei, P., Ma, Z., Xu, H., Li, P., Wang, X., 2014. Morphology control of zinc regeneration for zinc-air fuel cell and battery. *J. Power Sources* v271. <https://doi.org/10.1016/j.jpowsour.2014.07.182>.
- Wang, H., Zhang, P., Wang, K., Zuo, Y., Wei, M., Chen, Z., Shang, N., Pei, P., 2023. A self-designed double cross-linked gel for flexible zinc-air battery with extreme conditions adaptability. *J. Chem. Eng.* v451 <https://doi.org/10.1016/j.cej.2022.138622>.
- E. Wood, K.N., Kazzyk, E., Chadwick, A.F., Chen, K.-H., Zhang, J.-G., Katsuyo, T., Dasgupta, N.P., 2016. Dendrites and pits: untangling the complex behavior of lithium metal anodes through operando video microscopy *ACS Cent. Sci.* v2 <https://doi.org/10.1021/acscentsci.6b00260>.
- Yang, X., Wang, J., Zhao, W., Dou, H., Wan, B., Zhang, Y., Li, W., Zhao, X., 2020. Electrostatic shielding guides lateral deposition for stable interphase toward reversible magnesium metal anodes. *ACS Appl. Mater. Interfaces*, v12. <https://doi.org/10.1021/acsami.0c03603>.
- Yang, C., Zou, P., Sui, Y., Zhan, H., Wang, C., Xin, H.L., Cheng, H.-M., Kang, F., 2021. Polymorph evolution mechanisms and regulation strategies of lithium metal anode under multiphysical fields. *Chem. Rev.* v21 <https://doi.org/10.1021/acs.chemrev.0c01100>.
- Yassine, M.M., Dires, A.G., Lucy, C.A., 2007. Semipermanent capillary coatings in mixed organic-water solvents for CE. *Electrophoresis* v8. <https://doi.org/10.1002/elps.200600440>.
- You, Y., Yang, C., Xin, S., Mai, L., 2021. Materials design for high-safety sodium-ion battery. *Adv. Energy Mater.* v11 <https://doi.org/10.1002/aenm.202000974>.
- Yu, X., Guo, M., Yuan, C., Zhang, T., 2022. Solid-state electrolytes for rechargeable magnesium-ion batteries: from structure to mechanism. *Small.* <https://doi.org/10.1002/sml.202106981>.
- Zeng, W., Guo, Q., Liu, S.-L., Li, Y.-Q., Xu, J.-Y., Wang, J.-X., Wang, Y., 2021. Recent developments on anode materials for magnesium-ion batteries: a review. *Rare Met.* v40 <https://doi.org/10.1007/s12598-020-01493-3>.
- Zhao, C., Lu, Y., Yue, J., Pan, D., Qi, Y., Hu, Y.-S., Chen, L., 2018. Advanced Na metal anodes. *J. Energy Chem.* v27 <https://doi.org/10.1016/j.ijechem.2018.03.004>.
- Zhu, G., Sun, H., Zhu, Y., Lin, M.-C., Chen, H., Li, Y.-Y., Hung, W.H., Zhou, B., Wang, X., Bai, Y., Gu, M., Huang, C.-L., Tai, H.-C., Xu, X., Angell, M., Shyue, J.-J., Dai, H., 2020. High-safety and high-energy-density lithium metal batteries in a novel ionic-liquid electrolyte. *Adv. Mater.* v32 <https://doi.org/10.1002/adma.202001741>.